Shipu Han, Zhiwei Sun, Zhao Feng Tian, Timothy Lau and Graham Nathan

Particle velocity measurement within a free-falling particle curtain using microscopic shadow velocimetry

Optics Express, 2021; 29(7):10923

DOI: http://dx.doi.org/10.1364/oe.421017

Research Article | Vol. 29, No. 7 / 29 March 2021 / Optics Express 10923
Optics EXPRESS

Particle velocity measurement within a free-falling particle curtain using microscopic shadow velocimetry

SHIPU HAN,[1] ZHIWEI SUN,[1,*] ZHAO FENG TIAN,[1] TIMOTHY LAU,[1,2] AND GRAHAM NATHAN[1]

[1] *Centre for Energy Technology (CET), School of Mechanical Engineering, The University of Adelaide, S.A. 5005, Australia*
[2] *UniSA STEM, University of South Australia, Australia*
[*] *zhiwei.sun@adelaide.edu.au*

Abstract: We report an optical method for particle velocity measurement that is suitable for the measurement of particle velocities within dense particle-laden flows with high spatial resolution. The technique is based on particle shadow velocimetry with the use of a long-distance microscopic lens for images collection. The narrow depth of field of the lens allows particles within the focal plane to have much higher pattern intensities than those outside it on the collected images. Data processing was then employed to remove particles from outside the focal plane based on the gradient of the signal and a threshold. Following this, particle velocity was calculated from two successive images in the usual way. The technique was successfully demonstrated in a free-falling particle curtain with volume fractions in the four-way coupling regime of near-spherical micro-particles falling under gravity. The method was successfully employed to measure the transverse velocity profile through the curtain, which is the first time that such a measurement has been performed. Other highly-fidelity experimental data, which is also well suited to model development and validation, include the particle mass flow rate, curtain thickness and opacity.

1. Introduction

There is an ongoing need for high-fidelity experimental data in particle-laden flows to increase understanding of the complex interactions between fluid and particles, particularly in conditions with high particle loadings in the four-way coupling regime [1]. Such data are needed to guide the development and validation of predictive models for applications including novel, high-temperature solar thermal receivers [2–4], minerals processing [5–7] and food processing [8–10]. In the application of solar-particle receivers, the particles fall through an opening at the base of a tapered hopper, leading to particle volume fractions in the range of some 1% to 60% and path lengths sufficient to yield opacities in the range of 0.1 to 0.9 [2,3,11]. These high values are desirable to achieve sufficient absorption of the concentrated radiation but also lead to strong interactions between each other and with the gas phase, as the particle curtain evolves in time and space. This densely laden flow regime, termed the four-way coupling regime [1], is still poorly understood compared with the one- and two-way coupling regimes, both of which have much lower particle loadings, which limits capacity to develop reliable models. The lack of reliable data can be attributed to significant challenges of performing reliable measurements of both gas and particle velocities in the presence of such high particle loadings. The distributions of number-density and velocity are important because they control both the particle dispersion and gas-phase entrainment, which in turn have a controlling influence on heat transfer and residence time in the receivers [4,12–15]. Consequently, there is a need to develop improved measurement

#421017 https://doi.org/10.1364/OE.421017
Journal © 2021 Received 27 Jan 2021; revised 11 Mar 2021; accepted 12 Mar 2021; published 23 Mar 2021

Optics EXPRESS

techniques to provide reliable and well-resolved measurement of these parameters in particle laden flows within the four-way coupled regime.

Particle image velocimetry (PIV) is widely used for velocity measurement in particle-laden flows with moderate volume fractions, because they can be non-intrusive and provide high spatial resolution [16,17]. The most common method to achieve spatial resolution within such a flow is to illuminate the particles with pulsed light sheets and then determining the correlation between the subsequent images of scattered light. The gas velocity can also be measured with tracer particles for the case where the particles have a sufficiently small Stokes numbers, i.e., the ratio of particle response time to the flow time scale $S_t = \tau_p \,/\, \tau_{flow} < 0.05$ [18]. Particle-tracking velocimetry (PTV) is as a complementary tool, but can only be employed for very low volume fractions [16]. However, PIV becomes unreliable where the particle volume fraction and optical path length become too high, owing to the strong effects of laser scattering, which leads both to the broadening and attenuation of both the laser sheet and the signal [19]. Hence, in conditions such as a falling particle curtain, the spatial resolution is too degraded and the signal too attenuated to be useful. Hence, the only PIV images available for a falling particle curtain have been obtained from images with illumination of the entire sheet [3], so that they lack spatial resolution. Several techniques were proposed to image microscopic objects within the optically-dense multi-phase flows, particularly in the core region of sprays, by suppressing multiple-scattering noises based on time gates (ballistic imaging [20–22]), structured illumination (structured laser illumination planar imaging, or SLIPI [23,24]) and interferometry (e.g., off-axis holography [25]). However, in these techniques, ballistic imaging cannot provide spatial resolution in the beam-propagation direction [20], while SLIPI has yet demonstrated in highly dense droplet or particle flows [24]. The off-axis holography also has a low spatial resolution in the beam-propagation direction, which was reported as several centimeters even using a femtosecond light source [25]. All of these are barriers to their applications for the present purpose. For this reason, there is a need for new methods that are capable of providing spatial resolution within the curtain.

Particle shadow velocimetry (PSV) is another non-intrusive optical method that has been developed for the measurement of velocities of microparticles, bubbles and droplets [19,26–28]. In this method a backlight is used to generate shadows from the object, so that the displacement of the object can be derived from successive shadow images recorded with a modulated light source. A limitation of conventional PSV is the line-of-sight nature of the signals, which prevents spatial resolution in the viewing direction. However, this can potentially be overcome by use of an imaging system with a short depth-of-view (DoF) together with a thresholding and filtering process based on the fact that the darkness of the object shadow decreases on the out-of-focus plane [29]. Nevertheless, while this method has been demonstrated in flows such as those laden with small transparent airborne particles (a few of micrometers), bubbles and droplets [19,26–28], all of these have much lower volume fractions (in one-way coupling regime) than occur in free-falling particle curtains and negligible attenuation. For these reasons, the extent to which reliable signals could be obtained from the conditions in a falling curtain or can be reliably distinguished from particles in different planes with the thresholding method, is yet to be determined. Furthermore, the spatial resolution that can be achieved with microscopic PSV (μ-PSV) in the viewing direction has yet to be quantified within such environments.

Specific to the free-falling particle curtain proposed for solar receivers, the flow field is conceptually simple (at least in the absence of wind) as the particles are much heavier than air. The dominant component of the particle velocity is therefore aligned with gravity, consistent with the observation that the curtain thickness increases only slightly with the falling distance from the hopper [2,3]. This nominally two-dimensional velocity field is an ideal environment for the development and demonstration of μ-PSV because of the weak out-of-plane velocity components. That is, it is well-suited to also assess the effectiveness of a further step in the image processing

Optics EXPRESS

method to filter out-of-focus signals with a view to further improving the spatial resolution in the viewing direction.

In light of the discussion above, the overall aim of the present investigation is to develop the micro-PSV technique to achieve high spatial resolution for the measurement of the particle velocities within the high volume loading conditions that apply in free-falling particle curtains. In particular we aim to quantify the resolution that can be achieved with various optical configurations and image process methods in these environments. In addition to particle velocity, we further aim to assess the efficacy of the method in measuring curtain opacity, thickness and particle mass flow rate.

2. Experiments

2.1. Optical setup

Figure 1 presents a schematic diagram of the experimental arrangement, comprising a micro-PSV system and a curtain of particles free falling from a hopper with a rectangular orifice into a quiescent environment. A high-power LED array (SOLIS-365C) with a wavelength of 365 nm was used as the backlight for illumination. The LED array has a maximum power of 4W under continuous operation, but here was trigged with an external signal generator to operate in a dual pulse mode at a repetition frequency of 2 Hz. The duration of each pulse was approximately 5 µs with a time-delay of 33 µs between them. (A temporal profile is shown in the Supplement 1). The power of each LED pulse was too low to be measurable, but its fluorescence was clearly visible on white paper. On the other side of the particle curtain, the particle shadow was imaged using a long-distance microscopic lens (LM100) onto a dual-frame PIV camera (PCO.2000), which was synchronized with the LED light source. Therefore, two subsequent particle shadow images can be recorded with a time interval of 33 µs for velocity derivation. The image system has a field of view (FoV) of 3.5×3.5 mm^2, corresponding to 1.7 µm/pixel. According to the specification provided by the manufacturer, the DoF of the microscopic lens is approximately 0.155 mm and the f-number is 8.7. The microscopic imaging system was traversed horizontally in steps of 1 mm, i.e., along the y direction as shown by the coordinate system in Fig. 1, enabling different planes within the particle curtain to be imaged. The spatial resolution of the experimental method in the y direction was also assessed by imaging fixed microparticles, which were mounted to a flat quartz plate. This was traversed with a micro-translation device across the focal plane of the imaging system.

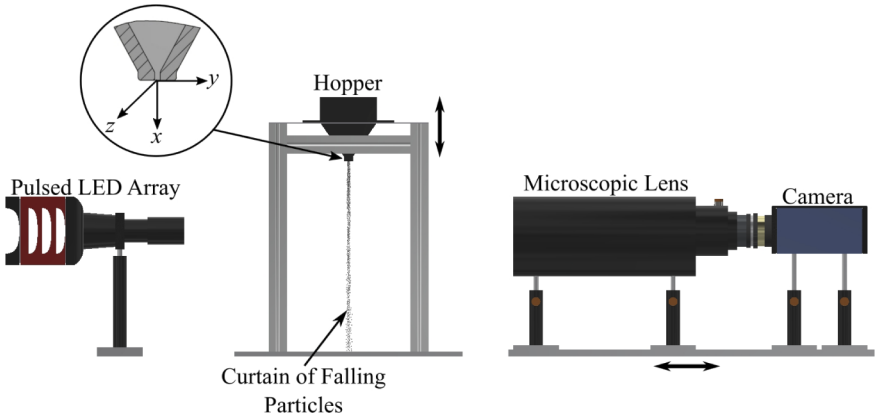

Fig. 1. Schematic diagram of the experiment arrangement employed for microscopic particle shadow imaging.

Optics EXPRESS

2.2. Hopper and particles

A wedge-shaped discharge hopper was used in the present work with a slot aperture at the exit plane of 2 mm × 40 mm, whose details can be found in the Supplement 1. Carbo CP 70/140 particles (Carbo Ceramics Inc.), with properties summarized in Table 1, were fed through the hopper to generate a free-falling particle curtain. The mass flow rate of the particles was measured by weight loss using a container mounted on a digital scale located at the base of the falling curtain to collect the particles following previous work with falling particle curtains [2]. This approach adapts the Beverloo equation [30,31] for flow through hoppers, which reach a steady flow-rate within a very short time to provide a reliable measurement [2]. To minimize errors, measurements were repeated five times. The shadow of the curtain was recorded using a white LED planar light source and a CCD camera aligned normal to it, from which the transmission of the curtain was calculated. The typical run time of the curtain was approximately 22 seconds and all measurements were conducted during the middle of the run, when the curtain had reached steady state.

Table 1. Carbo CP 70/140 particle properties[a]

Property	Value
Composition	Sintered bauxite
Mass-median diameter, d_p (μm)	154
Diameter distribution (μm)	74–105: 5%;
	105–149: 43%;
	149–212: 51%;
	212–300: 1%
Bulk density, ρ_{pb} (kg/m^3)	1890
Density, ρ_p (kg/m^3)	3250

[a]From www.carboceramics.com

3. Data processing methodology

Figure 2 presents a flow chart of image processing to identify the particles on the focal plane and filter out those that are out of the plane. The methodology is based on the principle that the particles on the focal plane are sharply imaged, while those out of the focal plane are blurred. Hence, the magnitude of the gradient of intensity at the particle edge is greater than those out of the focal plane. Briefly, the imaging process comprises the following steps:

(1) A raw shadow image, matrix $I(i, j)$, is loaded without subtracting the background. The 2D gradient of the image, G, is then calculated by taking the first derivative of the intensity value across the image with the following equations [32]:

$$G(i,j) = [G_i, G_j] = \nabla I(i,j) = \left[\frac{\partial I}{\partial i}, \frac{\partial I}{\partial j}\right], \tag{1}$$

$$\left|G(i,j) = \sqrt{{G_i}^2 + {G_j}^2}\right|, \tag{2}$$

$$\theta(i,j) = \arctan\left(\frac{G_j}{G_i}\right), \tag{3}$$

where $|G(i, j)|$ and $\theta(i, j)$ are the magnitude and direction of the gradients. A 2D Gaussian filter is then applied to Image G to smooth it.

Optics EXPRESS

(2) The probability density function of the pixel intensities was calculated for the entire set of images G, and a threshold value ε was determined by multiplying a threshold constant, c, with the mean of the ten largest values in $G(i, j)$, termed as $I_{\max}$, as follows:

$$\varepsilon = cI_{\max}, \tag{4}$$

where c ranges from 0 to 1.

(3) The threshold value ε was applied to G for image filtering, resulting in Image B that was processed as follows:

$$B(i,j) = \begin{cases} 0, & G(i,j) \le \varepsilon \\ G, & G(i,j) > \varepsilon \end{cases}, \tag{5}$$

(4) The edges of the particles identified in this way, which are deemed to be within the thin focusing plane, were used to calculate the particle velocity from a pair of images $B(0)$ and $B(\Delta t)$. This process was conducted by cross correlation using an evaluation window of 512 × 512 pixels with an overlap of 50% via the open-source software of PIVlab [33]. This window size corresponds to about 5 diameters of the 154-μm Carbo CP particles, whose diameter typically has a diameter of around 100 pixels in each image, while the typical displacement between frames ranges from 15 to 50 pixels. The final results were found to be insensitive to the size of the correlation window.

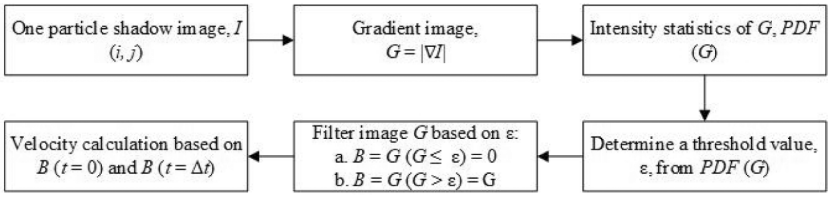

Fig. 2. Flow chart of the data processing steps employed to identify particles within the focal plane and calculate velocity.

A further processing step was applied to those processed images for which the number of particles identified after gradient thresholding is low, which can occur either for cases with very high particle loading (causing shadows to overlap) or to very low particle loading (resulting in few particles within the image plane). This additional processing step, shown in Fig. 3 as Step 2, was applied where necessary to increase the number of data points in the velocity calculation by superimposing the detected particles from different parts of sub-images B with the same average velocity. This increases the number density of valid data from which velocity vectors can be calculated. The option splits Image B into four vertical sub-images in the x direction and then superimposes them to form a single image with more dense valid data. This is valid because the curtain is planar, so that gradients in the z direction are nominally zero.

The accuracy of the velocity measured in the present work was assessed by comparing the j index (x direction) of valid pixels ($B \neq 0$, shown with dark color on an image) in filtered images with the temporally offset images, C_1 and C_2. Image $B(0)$ was shifted numerically along the x direction based on the velocity V_p (the mean value derived from a pair of images) and the time duration Δt, leading to an Image of C_1. Similarly, Image $B(\Delta t)$ was also shifted based on reverse

Optics EXPRESS

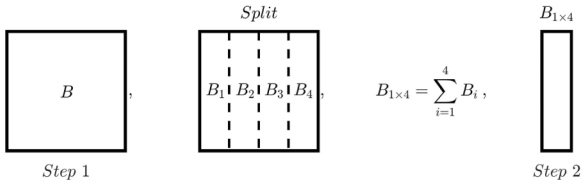

Fig. 3. Schematic diagram of the optional Data Densification Method used to superimpose subsections of the image with the same velocity to increase the number of data points available in interrogation windows for PIV calculations.

velocity (-V_p), generating an Image of C_2. This is expressed mathematically as follows:

$$C_1(i,j) = B(0)(i, j - f(V_p, \Delta t)), \tag{6}$$

$$C_2(i,j) = B(\Delta t)(i, j + f(V_p, \Delta t)), \tag{7}$$

where f is a linear displacement in the x direction in units of pixels. Images C_1 and C_2 can be understood as the translational projection of images of $B(0)$ and $B(\Delta t)$, respectively, based on the measured particle velocity. Therefore, the accuracy of the measured velocity can be assessed by comparing the valid j indices between Image $B(0)$ and Image C_2, or between Image $B(\Delta t)$ and Image C_1. For the ideal case in which the calculated particle velocity is identical to the true particle velocity, the indices of the particle location on x direction in $B(0)$ would be identical to those in C_2, and similarly for $B(\Delta t)$ and C_1. However, the ideal case only applies to perfectly spherical particles, as imperfect translation may arise due to the rotation of non-spherical particles during the time interval, which can generate spurious particle shadow patterns in the filtered images. For this reason, Image $B(0)$ and Image $B(\Delta t)$, and therefore Image C_1 and Image C_2, may not be identical, which means direct comparisons of valid indices between the filtered images and the temporally offset images may not be achievable. To solve this issue, two new index arrays, D_1 and D_2, that consist of the index of all valid pixels of the filtered and temporally offset images respectively, were then introduced and compared to assess the accuracy of the entire measurement, which is expressed mathematically as follows:

$$D_1(j) = [B_0(j); B_{\Delta t}(j)], \tag{8}$$

$$D_2(j) = [C_2(j); C_1(j)], \tag{9}$$

The ideal case now can be mathematically represented as $D_1(j) = D_2(j)$, which is a straight line with a linear equation of $y = x$.

4. Results and discussion

Figure 4 presents instantaneous images of the curtain recorded with an exposure time of 500 µs from two viewing directions with a large white LED plane as the backlight. The curtain exhibits negligible expansion in the lateral z direction as can be seen by comparison of the edge with a vertical red-dashed line [Fig. 4(a)] and only expands a few of millimeters in the transverse y direction [Fig. 4(b)]. The axial distance of this image is 480 mm in the x direction, which corresponds to $x = 240d$ (d is the thickness of the aperture, which is 2 mm). These observations indicate that the dominant velocity is the axial component, u, as is well know from previous investigations [2,3].

Figure 5 presents the thickness ($\delta_{0.1}$, defined as the distance between the axis of the curtain and edge, based on the point where the signal intensity is 10% of that on the axis), opacity (O), the mean of particle volume fraction (ϕ) averaged cross the thickness and particle mass flow rate

Optics EXPRESS

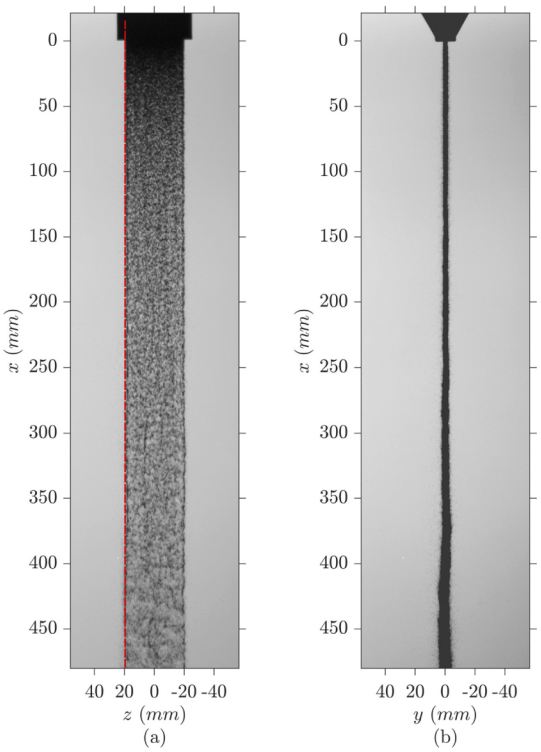

Fig. 4. Instantaneous images of the free-falling particle curtain from (a) a front view and (b) a side view.

($\dot{m}$) of the curtain. These characteristics are obtained from analysis of the front and side views of the curtain and details are presented in the Supplement 1. The values at six specific heights are highlighted, corresponding to the heights at which the particle velocities were measured using the μ-PSV. Figure 5 shows that the curtain has a constant mass flow rate of 20.2 g/s, and it gradually expands from 2.13 mm near the hopper to approximately 7 mm at $x = 480$ mm, resulting in a corresponding decrease in the opacity and the spatial-averaged particle volume fraction along the fall height. However, Fig. 5(d) shows that the volume fraction ranges from 0.01 to 0.1, which indicates that the curtain is in the four-way coupling regime [34].

Figure 6 shows a representative series of the images generated in data processing for deriving the particle velocity at the fall height of 460 mm. As shown in Fig. 6(a), the particles on the focus planes are sharply imaged, while those out of the focus plane are blurred and their shadows become transparent. These particles on, and near to the focal plane can have large intensities in the raw image and steep intensity gradients after derivation. Therefore, the gradient images [Figs. 6(b) and 6(c)], which were derived from the first derivative of the raw images, show that these steep intensity gradients result in large intensity magnitudes and clear particle boundaries.

Two mathematical operators, the Sobel and Prewitt operators, were applied to the raw images to compare the influence of the choice of gradient calculation algorithms on particle velocities. These operators are both commonly used edge detection algorithms that use two 3×3 convolution masks in horizontal and vertical directions to approximate the gradient of an image, resulting in the following equations to be used instead of Eq. (1) to calculate the gradient [35]:

$$G_i = (a_2 + na_3 + a_4) - (a_0 + na_7 + a_6), \tag{10}$$

$$G_j = (a_0 + na_1 + a_2) - (a_6 + na_5 + a_4), \tag{11}$$

Optics EXPRESS

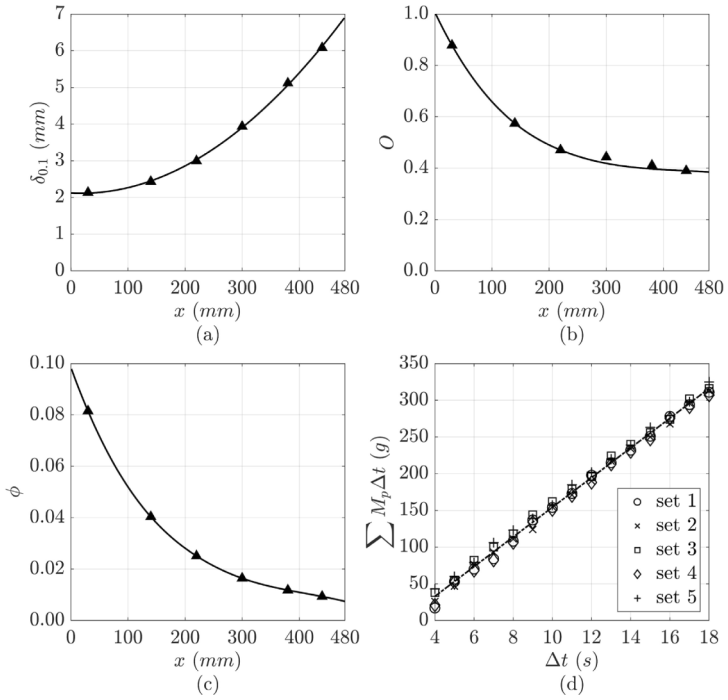

Fig. 5. Axial distributions of: (a) radial width of the curtain based on the 10% signal intensity, or curtain thickness (b) curtain opacity, and (c) particle volume fraction averaged across the curtain thickness. Also shown is (d) the mass of particles collected at the base of the curtain as a function of time.

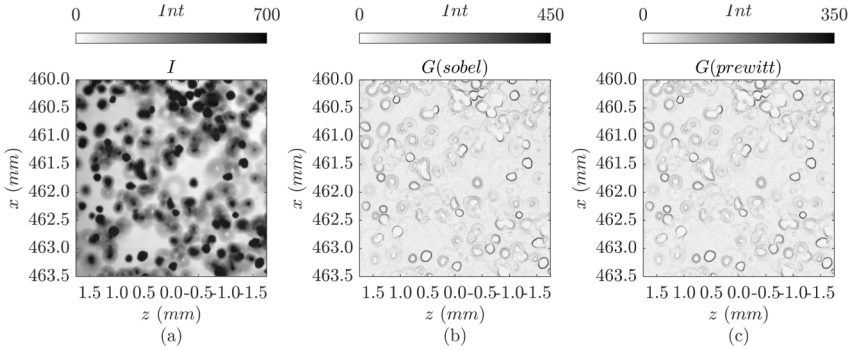

Fig. 6. An illustration of the data processing method at $x = 460$ mm and $y = -0.63$ mm, showing (a) a representative raw image of particle shadows; (b) the magnitude of intensity gradients of the image obtained with the Sobel algorithm; (c) the magnitude of intensity gradients of the image obtained with the Prewitt algorithm.

where a_0 to a_7 are labels in the 3×3 region of an image (labelling clockwise from the up-left corner), and n is a constant, which is $n = 1$ for the Prewitt operator and $n = 2$ for the Sobel operator. Comparing the gradient images obtained with Sobel and Prewitt operators [shown in Figs. 6(b) and 6(c)], the only difference between the two figures is the intensity magnitudes, i.e., the gradient images obtained with the Sobel operator has larger intensity magnitudes than those obtained with the Prewitt operator. This result is consistent with the previous finding that the Sobel operator gives more weight to the pixel values around edges and thus increases the edge intensity [36].

Optics EXPRESS

To further detect the influence of gradient calculation algorithms, two groups of the raw images, collected at $x = 460$ mm, $y = -0.63$ mm and -7.63 mm respectively, were selected and processed with both the Sobel and Prewitt operators. The same value of the threshold constant $c = 0.6$ was selected to filter the gradient images obtained from both operators and particle velocities were calculated based on the corresponding filtered images. Particle velocities obtained based on images collected at $y = -0.63$ mm and -7.63 mm and processed with the Sobel operator are 2.7424 m/s and 2.0221 m/s, respectively, while those processed with the Prewitt operator are 2.7415 m/s and 2.0054 m/s. Neglectable velocity difference can be found for the selected cases, indicating the particle velocity is almost independent from the choice of the gradient calculation algorithm. Nevertheless, because the Sobel operator has been reported to have a better edge detection efficiency and to provide sharper edges [36], this was selected for further image processing.

Figure 7 presents the raw images, the corresponding gradient images, and the filtered images obtained with the threshold constant, c [Eq. (4)], varied from 0.2 to 0.8. To comprehensively represent the free-falling curtain, images collected at similar transverse position (centre of the curtain) but different fall heights ($x = 30$ mm, 220 mm and 460 mm) and the same fall height ($x = 140$ mm) but different transverse distances ($y = -0.52$ mm, -2.52 mm and -3.52 mm) were assessed. It can be observed that the background noise is large for small value of the threshold constant, i.e., $c = 0.2$, due to incomplete filtration of out-of-focus particles. Furthermore, some in-plane particles are removed with a large threshold constant values, i.e., $c = 0.8$, resulting in less valid data on the images for PIV analysis. Observing from the gradient images and the filtered images at $x = 140$ mm $y = -3.52$ mm and -2.52 mm in Fig. 7, most outside-plane particles can be filtered with $c = 0.4$, while particles locate near to the focal plane were partially removed. As a result, the suitable range for c is between 0.4 and 0.8, and to find a more precise value further processes were applied.

Figure 8 presents the values of mean and RMS (in percentage) of particle velocities (V_p), together with the valid pixel numbers obtained from the filtered images with threshold values $c = 0.4$, 0.5, 0.6 and 0.7. These were obtained from images collected at a fall distance of $x = 140$ mm, which corresponds to $x/d = 70$, and the RMS velocity was calculated by the open-source software PIVlab using the following equation:

$$RMS = \left(\frac{\sum_{i=1}^{N} (V_i - V_m)^2}{N} \right)^{\frac{1}{2}} \tag{12}$$

where N is the total number of image pairs, V_i is the velocity of the i-th image, and V_m is the mean velocity of N image pairs. At this distance the velocity at the edge of the curtain is measured to be approximately half that at the axis, which is consistent with the limited amount of data available in such flows. While the velocity at the hopper exit plane is typically close to uniform, even there the effects of wall friction cannot be ignored [37], resulting in some reduction in velocity at the curtain edge further downstream. The influence of aerodynamic shear in reducing the velocity of the curtain close to the jet edge have been observed previously [2,3] and can be expected to becomes increasingly significant with axial distance. While these non-uniform particle velocity profiles are well-known in particle-laden jets [38], they have not previously been measured in a dense falling particle curtain.

It can also be seen from Figs. 8(a) and 8(b) that the measured values of mean and RMS velocity agree for all values of c in the middle of the jet ($-1.5 < y < 1.5$ mm) and converge throughout the jet for $c = 0.6$ and 0.7. The collapse of the measurements for all values of c in the middle of the jet can be attributed to the uniform velocity in the lateral direction there, so that any out-of-focus particles have the same velocity as the in-plane particles. The differences in the measurement at the edge of the jet can be attributed to the out-of-focus particles having a different velocity than the in-focus particles due to the lateral velocity gradient at the edge of the jet. That is, a small number of particles that are suspended in the entrained, ambient fluid are also entrained

Optics EXPRESS

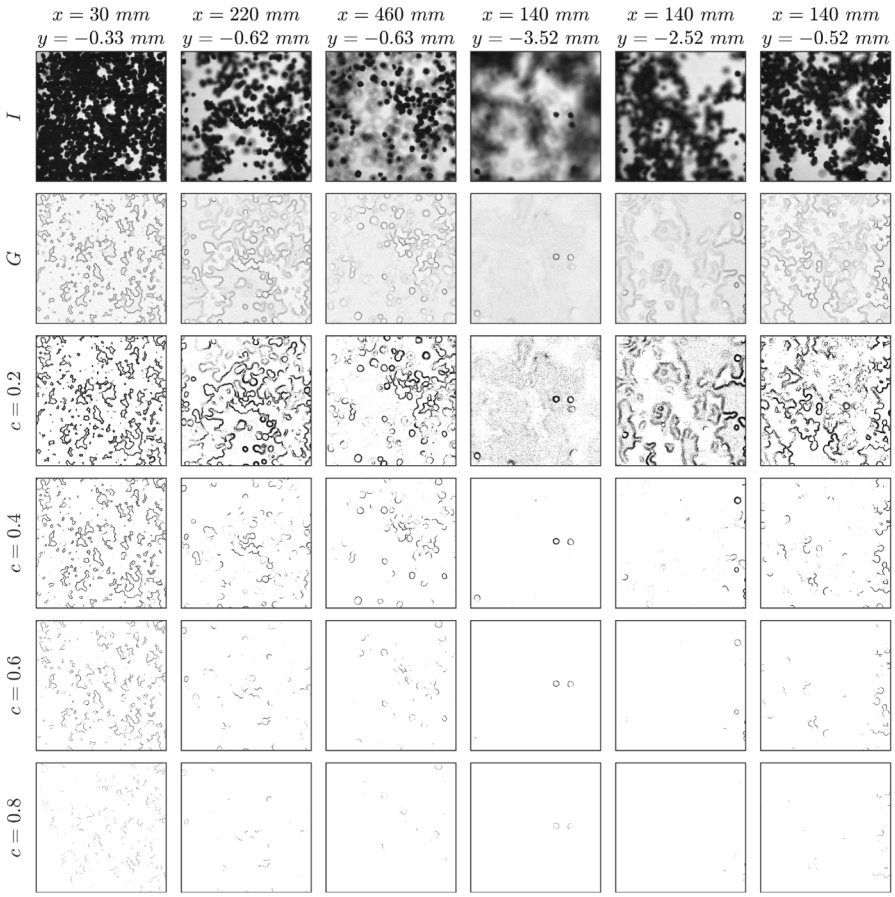

Fig. 7. A systematic assessment of the selection of the threshold constant, c (Eq. (4)), for images collected at different fall heights (x) and transverse distances (y). The first row presents the raw images of free-falling particles, while the second row presents the corresponding gradient images. The other rows present the filtered images obtained with various values of the threshold constant, c.

into the jet. These have a relatively high transverse velocity and a relatively low axial velocity. The good agreement for different values of the threshold shows that use of $c = 0.6$ is sufficient to remove the out-of-plane particles from the measurement. It also shows that the relatively simple cross-correlation algorithms used here are sufficiently accurate for the present flow, consistent with its high degree of uniformity and axial direction of the particles that originate from the curtain.

The explanation above also explains the increase in RMS of measured particle velocities at the edge of the curtain with a reduction in the value of c, as shown in Fig. 8(b). Note that the measured value of RMS $\sim$ 1% is reasonable because some small variations can be expected due to aerodynamic effects. A trade-off between reduction in the measured value of RMS and the number of pixels with valid particles with an increase in value of the threshold constant [can be seen by comparing Figs. 8(b) with 8(c)]. The removal of out-of-plane particles with an increase in c from 0.4 to 0.6 reduces the number of valid data points together with the measured value of RMS. The net effect is that values of $c = 0.6$ and 0.7 yield a sufficient number of particles for a reliable measurement of mean velocity within a narrow focal plane for this environment.

Optics EXPRESS

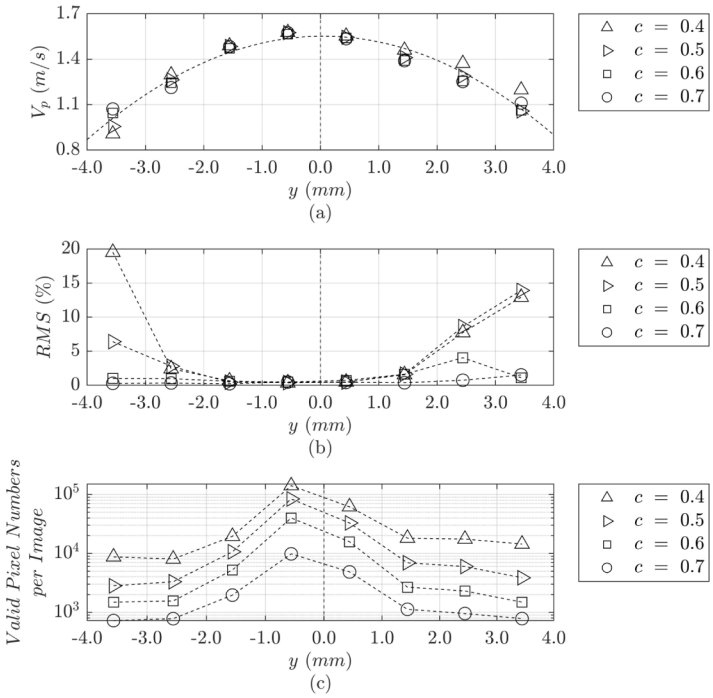

Fig. 8. Transverse distributions of (a) particle mean velocity; (b) percentage root-mean-square (RMS) velocity, and (c) number of valid pixels on each image obtained by averaging from the data set of 150 images for various values of the threshold constant, c (Eq. (4)) at $x = 140$ mm. The dashed line in Fig. 8(a) was derived from a truncated Gaussian distribution curve as suggested in Ref. [39].

Figures 9(a) and 9(c) present the correlations between the indices of valid pixels for one pair of the filtered and temporally offset images ($D_1(j)$ and $D_2(j)$, obtained with Eqs. (8) and (9) with the threshold values of $c = 0.6$ and 0.7 respectively). It can be seen that a high degree of overlap occurs between the filtered and temporally offset images for both threshold values. This indicates a high degree of accuracy for the velocity measurement. Figures 9(b) and 9(d) present the differences between the correlations and the ideal case $D_1(j) = D_2(j)$ for pixels and normalized velocities ($\Delta V_p/V_p$). A difference of ± 1.5507 pixels or ± 0.0504 of the normalized velocity relative to the ideal case was derived from Fig. 9(b) for $c = 0.6$, while that of ± 2.6204 pixels or ± 0.0852 normalized velocity was derived from Fig. 9(d) for $c = 0.7$. These values represent the typical accuracy of the velocities measured using this μ-PSV technique, and also show that $c = 0.6$ is the most suitable value of the threshold constant.

Figure 10 presents the gradient images obtained for the assessment of spatial resolution in the out-of-plane direction. This shows raw and filtered images of particles that were obtained from viewing a fixed distribution of particles mounted to a flat quartz plate that was translated laterally from the focal planes by various distances $\Delta y = y - y_0$. The filtered images are shown for a series of threshold values, i.e., various values of c. It can be seen that the range of Δy, in which the particles can be identified for velocity derivation, depends on the value of c, as expected. A larger value of c leads to a thinner detection volume, i.e., a higher spatial resolution in the y direction. In the present work, a value of 0.6 was chosen, corresponding to a resolution of $\Delta y = \pm 0.5$ mm. That is, a spatial resolution in the viewing direction of better than ± 0.5 mm can be obtained with this method.

Optics EXPRESS

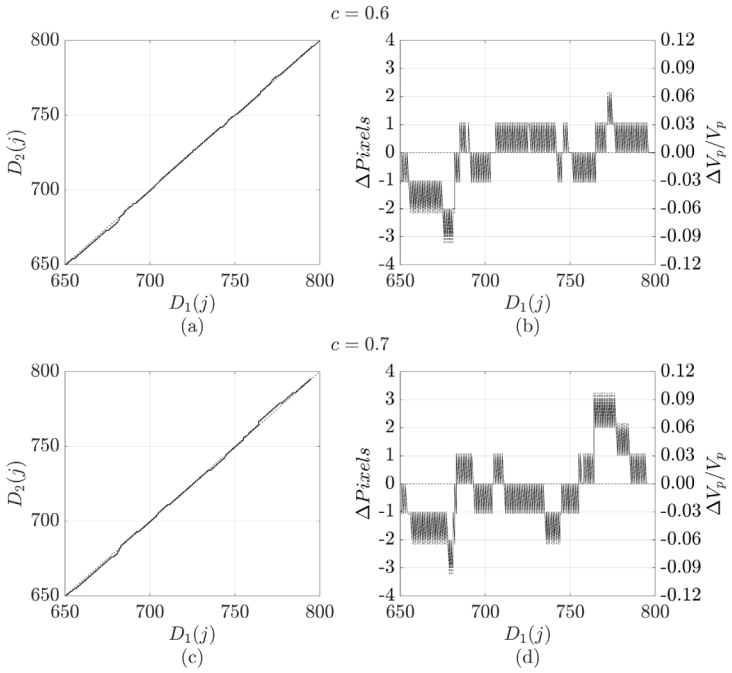

Fig. 9. An assessment of the accuracy of the μ-PSV technique using $D_1(j)$ and $D_2(j)$, from Eqs. (8) and 9, for two values of the threshold constant at $x = 140$ mm, $y = -0.52$ mm, showing (a) the correlation between the indices of valid pixels in pairs of the filtered and temporally offset mages for $c = 0.6$; (b) the difference between the correlation and the ideal case, $D_1(j) = D_2(j)$, in the units of pixel and normalized velocity with $c = 0.6$; (c) the equivalent correlation for $c = 0.7$, and (d) the equivalent difference for $c = 0.7$.

Figure 11 presents the relationships between the threshold constant c, the spatial resolution Δy and the number of valid pixels after image processing. It can be seen from Fig. 11(a), that the spatial resolution increases, that is the value of Δy decreases from 1.3 to 0.3 mm, as the value of c is increased from 0.2 to 0.9. However, the corresponding number of valid pixels also decreases asymptotically toward zero for the same increase in c, consistent with Fig. 8(c). This also shows that a good trade-off seems to occur for $c = 0.6$, corresponding to $|\Delta y| = 0.5$ mm. Furthermore, Fig. 11(a) shows that a spatial resolution of $\Delta y = \pm 0.3$ mm across the curtain thickness is potentially achievable using this μ-PSV setup, although the number of valid pixels is low for this case.

Figure 12(a) presents the profiles of mean particle velocity across the thickness of the curtain for a series of fall heights, while Fig. 12(b) presents the axial evolution of the velocity on the central plane of the curtain. All the results were averaged over 150 images. The trends in Fig. 12(b) are consistent with those measured previously [2,3], and are agree to the predicted falling particle velocity by integrating Newton's second law of motion without air drag, with the equation $V_p=(2gx)^{0.5}$ [2]. However, the lateral profile through the curtain has not been measured previously. These reveal for the first time that the velocity varies by some 30% through the transverse direction, which is consistent with the relatively weak drag force within the curtain [2,15]. The difference is significant, with the difference being as high as ~ 40% at $x = 140$ and 220 mm. For the fall height of $x > 300$ mm the centre-line velocity approaches the terminal velocity of 3.37 m/s for the Carbo particles from the equation $V_{\text{terminal}} = \sqrt{2mg/\rho_f A C_d} = \sqrt{4d_p\rho_p g/3\rho_f C_d}$, where d_p and ρ_p are the diameter and density of the Carbo particles, respectively, $\rho_f = 1.225$ kg/m^3 is the density of air, and $C_d = 0.47$ is the drag coefficient of sphere. In addition, Fig. 12(a)

Optics EXPRESS

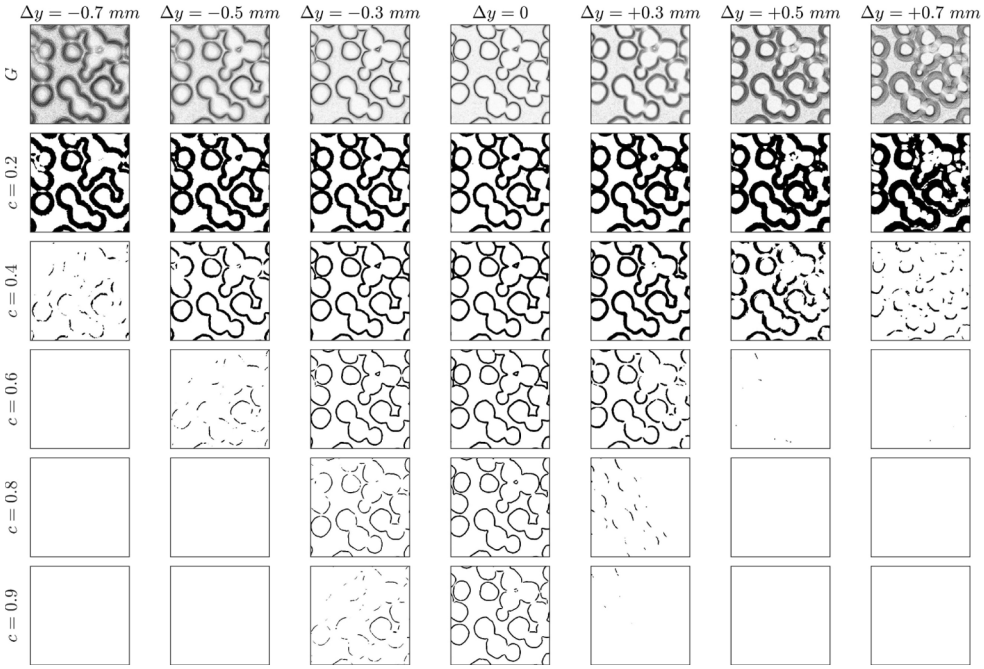

Fig. 10. A systematic assessment of the sensitivity is the method to the choice of thresholding constant on transverse spatial resolution. The first row presents the gradient images of particles mounted to a flat quartz plate at a series of lateral distances from the focal plane ($\Delta y = y - y_0$), while the rows below present the filtered images obtained with various values of the threshold constant, c (Eq. (4)).

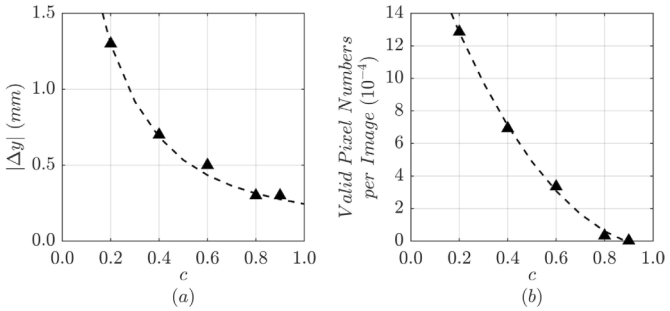

Fig. 11. Relationships between the threshold constant c and (a) absolute values of the spatial resolution$|\Delta y|$; (b) numbers of valid pixels on each of the filtered images at $|\Delta y| = 0$.

shows the symmetric profiles of the particle velocity across the curtain by the consistent results measured on both sides of the central plane, indicating the negligible influence of the particle loading on the measurement accuracy. Interestingly, Fig. 12(a) also shows that the particle velocities approach to a constant value of ~ 1.8 m/s at the edge of the curtain for the fall heights of $x = 300$ mm and 380 mm. Nevertheless, the number of the particles detected at the edge of the curtains is relatively low.

Figure 13 presents the measured values of transverse mean and RMS (in percentage) velocity profiles both with and without the additional Data Densification Process (Fig. 3) at the fall height of 300 mm. It can be seen that the additional processing step has little influence on most of the

Optics EXPRESS

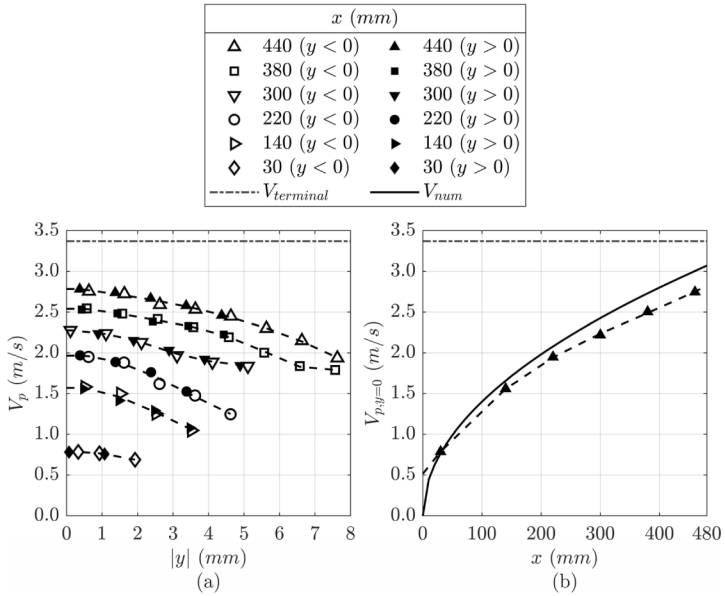

Fig. 12. (a) Transverse velocity profiles of particles across the span of the curtain at various fall heights, and (b) axial evolution of particle velocity on the central plane of the curtain. The solid line was obtained from Eq. (3) in Ref. [2].

results, which means that split then superimpose the filtered images has limited effect on increase the number density of valid data in interrogation windows for cross correlation. Nevertheless, the values of RMS are slightly lower and less scattered in the centre of the curtain, consistent with a reduction in noise associated with the increase in sample size. The slightly lower value of RMS at the edge of the particle curtain might be because of the gradient in the velocity at the edge of the curtain, to the increase in the number of measurement points. Nevertheless, the velocities are sufficiently close to each other to provide confidence in the data without the additional data densification process.

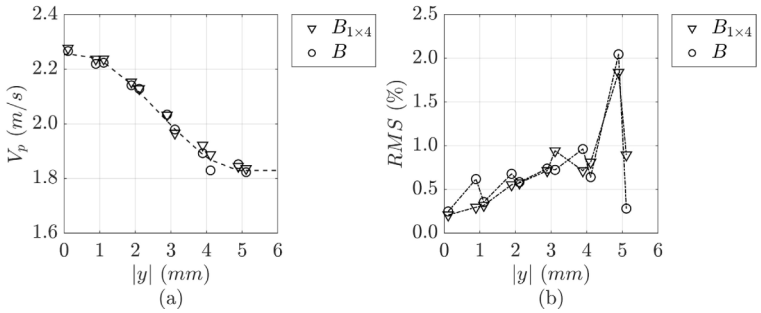

Fig. 13. (a) Axial profile of the particle velocities processed from the standard matrix B and via the image splitting method $B_{1\times4}$ at $x = 300$ mm, and (b) the corresponding RMS values.

5. Conclusion

The micro-focusing particle shadow velocimetry has been successfully applied to measure the velocity of particles of 154 μm diameter falling in a dense curtain under the influence of gravity

Optics EXPRESS

from a slot of 2 mm thickness with the opacity ranging from 0.4 to 0.9 and average particle volume fractions of a few percent, i.e., in the four-way coupling region. In addition to the quantitative data, which can be used for modelling validations, the main conclusions are as follows:

(1) A spatial resolution of better than ± 0.5 mm can be achieved in the viewing direction, i.e., in the transverse direction across the curtain. This is larger than the nominal DoF of 0.155 mm but is not very different from the typical resolution of a laser sheet measurement. The optical system has a FoV of 3.5×3.5 mm^2, corresponding to 1.7 μm/pixel, allowing resolution of individual particles and providing good resolution of particle velocity.

(2) The measurement of velocity was found to be insensitive to the values of the key parameters employed in the image processing process over a relatively wide range of conditions, providing confidence in the measurement. In particular, the detection of the edge of particles was relatively insensitive to the gradient calculation algorithm. Nevertheless, the value of the threshold constant needs to be optimized for each experiment, since it must be selected to give the best trade-off between the spatial resolution and the number of particles detected from the image. For the present conditions, the influence of the gradient calculation algorithm on calculated particle velocities was small for $c > 0.6$, while accuracy was affected for $c < 0.6$.

(3) While the limit of particle loading still needs to be assessed, the high accuracy of measured results and the independence of data processing variables indicate the micro-PSV technique works well in particle flows with interactions in the four-way coupling regimes and is suitable for measurements in dense particle-laden flows.

The method is potentially extendable to three dimensions using either multiple cameras and light sources or by consideration of gradients to detect out-of-plane motions. However, such extensions are beyond the scope of the present investigation.

Funding. U.S. Department of Energy through the G3-P3 project (DE-FOA-0001697); Australian Renewable Energy Agency through Australian Solar Thermal Research Institute; Australian Research Council (DP180102045).

Acknowledgments. Acknowledgment is given to Mr Xiaopeng Bi for the assistance in the experimental work of recording the curtain images.

Disclosures. The authors declare no conflicts of interest.

Data Availability. Data underlying the results presented in this paper are not publicly available at this time but may be obtained from the authors upon reasonable request.

Supplemental document. See Supplement 1 for supporting content.

References

1. S. Elghobashi, "On predicting particle-laden turbulent flows," Appl. Sci. Res. **52**(4), 309–329 (1994).
2. C. K. Ho, J. M. Christian, D. Romano, J. Yellowhair, N. Siegel, L. Savoldi, and R. Zanino, "Characterization of particle flow in a free-falling solar particle receiver," J. Sol. Energy Eng. Trans. ASME **139**(2), 1–9 (2017).
3. K. Kim, N. Siegel, G. Kolb, V. Rangaswamy, and S. F. Moujaes, "A study of solid particle flow characterization in solar particle receiver," Sol. Energy **83**(10), 1784–1793 (2009).
4. A. Kumar, W. Lipiński, and J. S. Kim, "Numerical modelling of radiation absorption in a novel multi-stage free-falling particle receiver," Int. J. Heat Mass Transf. **146**, 118821 (2020).
5. P. A. Shamlou, "Pneumatic conveying of bulk solids," Handl. Bulk Solids, 102–129 (1988).
6. T. Mathaba and X. Xia, "A parametric energy model for energy management of long belt conveyors," Energies **8**(12), 13590–13608 (2015).
7. J. G. Kim, I. S. Kang, S. S. Lee, and S. M. Jung, "Analysis of pneumatic transport of pulverized coal using solid phase velocity estimation method," Powder Technol. **230**, 188–192 (2012).
8. V. Ganesan, K. A. Rosentrater, and K. Muthukumarappan, "Flowability and handling characteristics of bulk solids and powders - a review with implications for DDGS," Biosyst. Eng. **101**(4), 425–435 (2008).
9. L. Sanchez, N. Vasquez, G. E. Klinzing, and S. Dhodapkar, "Characterization of bulk solids to assess dense phase pneumatic conveying," Powder Technol. **138**(2-3), 93–117 (2003).

Optics EXPRESS

10. J. Chen, S. K. Lau, L. Chen, S. Wang, and J. Subbiah, "Modeling radio frequency heating of food moving on a conveyor belt," Food Bioprod. Process. **102**, 307–319 (2017).
11. J. M. Hruby, B. R. Steele, and V. P. Burolla, "Solid Particle Receiver Experiments: Radiant Heat Test," Flux (1984).
12. C. K. Ho, J. M. Christian, J. Yellowhair, N. Siegel, S. Jeter, M. Golob, S. I. Abdel-Khalik, C. Nguyen, and H. Al-Ansary, "On-sun testing of an advanced falling particle receiver system," *AIP Conf. Proc.* 1734, (2016).
13. J. S. Kim, A. Kumar, W. Gardner, and W. Lipiński, "Numerical and experimental investigation of a novel multi-stage falling particle receiver," *AIP Conf. Proc.* 2126, 2012–2016 (2019).
14. C. K. Ho, J. M. Christian, J. E. Yellowhair, K. Armijo, W. J. Kolb, S. Jeter, M. Golob, and C. Nguyen, "On-Sun performance evaluation of alternative high-temperature falling particle receiver designs," J. Sol. Energy Eng. Trans. ASME **141**(1), 1–7 (2019).
15. Z. Liu, P. Cooper, and P. W. Wypych, "Air Entrainment by Free Falling Streams of Particles," *Australas. Fluid Mech. Conf.* (2004).
16. M. Raffel, C. E. Willert, S. T. Wereley, and J. Kompenhans, *Practical Image Veloimetry A Practical Guide*, 2nd ed. (Springer, 2018).
17. B. M. Wilson and B. L. Smith, "Uncertainty on PIV mean and fluctuating velocity due to bias and random errors," Meas. Sci. Technol. 24, (2013).
18. M. Samimy and S. K. Lele, "Motion of particles with inertia in a compressible free shear layer," Phys. Fluids A **3**(8), 1915–1923 (1991).
19. S. Khodaparast, N. Borhani, G. Tagliabue, and J. R. Thome, "A micro particle shadow velocimetry (μPSV) technique to measure flows in microchannels," Exp. Fluids 54, (2013).
20. M. Paciaroni and M. Linne, "Single-shot, two-dimensional ballistic imaging through scattering media," Nat. Photonics **43**(26), 5100–5109 (2004).
21. D. Sedarsky, J. Gord, C. Carter, T. Meyer, and M. Linne, "Fast-framing ballistic imaging of velocity in an aerated spray," Opt. Lett. **34**(18), 2748 (2009).
22. M. A. Linne, M. Paciaroni, J. R. Gord, and T. R. Meyer, "Ballistic imaging of the liquid core for a steady jet in crossf low," Appl. Opt. **44**(31), 6627–6634 (2005).
23. E. Berrocal, E. Kristensson, M. Richter, M. Linne, and M. Aldén, "Multiple scattering suppression in planar laser imaging of dense sprays by means of structured illumination," At. Sprays **20**(2), 133–139 (2010).
24. E. Kristensson, L. Araneo, E. Berrocal, J. Manin, M. Richter, M. Aldén, and M. Linne, "Analysis of multiple scattering suppression using structured laser illumination planar imaging in scattering and fluorescing media," Opt. Express **19**(14), 13647 (2011).
25. A. Ziaee, C. Dankwart, M. Minniti, J. Trolinger, and D. Dunn-Rankin, "Ultra-short pulsed off-axis digital holography for imaging dynamic targets in highly scattering conditions," Appl. Opt. **56**(13), 3736 (2017).
26. S. Khodaparast, N. Borhani, and J. R. Thome, "Application of micro particle shadow velocimetry μPSV to two-phase flows in microchannels," Int. J. Multiph. Flow **62**, 123–133 (2014).
27. S. M. Whitaker, D. Reilly, J. P. Bons, and J. Crafton, "A survey of airborne particle impact characteristics using high speed Particle Shadow Velocimetry," *43rd Fluid Dyn. Conf.* 1–17 (2013).
28. S. M. Whitaker, C. Sacco, and J. P. Bons, "Evaluation of coeffcients of restitution using high speed particle shadow velocimetry with application to particle separators for gas turbine engines," *52nd Aerosp. Sci. Meet.* 1–14 (2014).
29. J. Estevadeordal and L. Goss, "PIV with LED: Particle shadow velocimetry (PSV)," *43rd AIAA Aerosp. Sci. Meet. Exhib. - Meet. Pap.* 12355–12364 (2005).
30. W. A. Beverloo, H. A. Leniger, and J. Van de Velde, "The flow of granular solids through orifices," Chem. Eng. Sci. **15**(3-4), 260–269 (1961).
31. A. Janda, I. Zuriguel, and D. Maza, "Flow rate of particles through apertures obtained from self-similar density and velocity profiles," Phys. Rev. Lett. **108**(24), 248001 (2012).
32. D. Adlakha, D. Adlakha, and R. Tanwar, "Analytical Comparison between Sobel and Prewitt Edge Detection Techniques," Int. J. Sci. Eng. Res. **7**, 1482–1485 (2016).
33. W. Thielicke and E. J. Stamhuis, "PIVlab – Towards User-friendly, Affordable and Accurate Digital Particle Image Velocimetry in MATLAB," J. Open Res. Softw. **2**(1), e30 (2014).
34. M. Sommerfeld, *Numerical Methods for Dispersed Multiphase Flows* (Birkhäuser, Cham, 2017).
35. G. T. Shrivakshan, "A Comparison of various Edge Detection Techniques used in Image Processing," Int. J. Comput. Sci. Issues **9**, 269–276 (2012).
36. G. N. Chaple, R. D. Daruwala, and M. S. Gofane, "Comparisions of Robert, Prewitt, Sobel operator based edge detection methods for real time uses on FPGA," *Proc. - Int. Conf. Technol. Sustain. Dev. ICTSD 2015* 4–7 (2015).
37. S. Zhang, P. Lin, C. L. Wang, Y. Tian, J. F. Wan, and L. Yang, "Investigating the influence of wall frictions on hopper flows," Granul. Matter **16**(6), 857–866 (2014).
38. T. C. W. Lau and G. J. Nathan, "The effect of Stokes number on particle velocity and concentration distributions in a well-characterised, turbulent, co-flowing two-phase jet," J. Fluid Mech. **809**, 72–110 (2016).
39. Z. Q. Liu, "Air entrainment in free falling bulk materials," Dr. Philos. thesis (2003).